Journal of
Applied Crystallography
ISSN 0021-8898
Editor: **Anke R. Pyzalla**

A small/wide-angle X-ray scattering instrument for structural characterization of air–liquid interfaces, thin films and bulk specimens

U-Ser Jeng, Chiu Hun Su, Chun-Jen Su, Kuei-Fen Liao, Wei-Tsung Chuang, Ying-Huang Lai, Je-Wei Chang, Yi-Jiun Chen, Yu-Shan Huang, Ming-Tao Lee, Kuan-Li Yu, Jhih-Min Lin, Din-Goa Liu, Chia-Feng Chang, Chin-Yen Liu, Chien-Hung Chang and Keng S. Liang

J. Appl. Cryst. (2010). **43**, 110–121

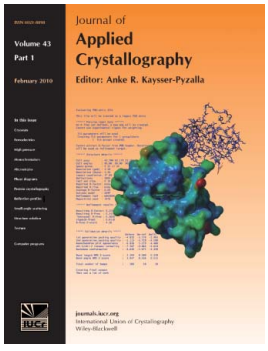

Journal of
Applied Crystallography
ISSN 0021-8898

Received 8 July 2009
Accepted 20 October 2009

A small/wide-angle X-ray scattering instrument for structural characterization of air–liquid interfaces, thin films and bulk specimens

U-Ser Jeng,[a]* Chiu Hun Su,[a] Chun-Jen Su,[a] Kuei-Fen Liao,[a] Wei-Tsung Chuang,[a] Ying-Huang Lai,[b] Je-Wei Chang,[b] Yi-Jiun Chen,[b] Yu-Shan Huang,[a] Ming-Tao Lee,[a] Kuan-Li Yu,[a] Jhih-Min Lin,[c] Din-Goa Liu,[a] Chia-Feng Chang,[a] Chin-Yen Liu,[a] Chien-Hung Chang[a] and Keng S. Liang[a]

[a]National Synchrotron Radiation Research Center, 101 Hsin-Ann Road, Hsinchu Science Park, Hsinchu 300, Taiwan, [b]Department of Chemistry, Tunghai University, Taichung, 407, Taiwan, and [c]Research School of Chemistry, Australian National University, Canberra ACT 0200, Australia. Correspondence e-mail: usjeng@nsrrc.org.tw

At the National Synchrotron Radiation Research Center, a small/wide-angle X-ray scattering (SAXS/WAXS) instrument has been installed at the BL23A beamline with a superconducting wiggler insertion device. This beamline is equipped with double Si(111) crystal and double Mo/B_4C multilayer monochromators, and an Si-based plane mirror that can selectively deflect the beam downwards for grazing-incidence SAXS (GISAXS) studies of air–liquid or liquid–liquid interfaces. The SAXS/WAXS instrument, situated in an experimental hutch, comprises collimation, sample and post-sample stages. Pinholes and slits have been incorporated into the beam collimation system spanning a distance of ~5 m. The sample stage can accommodate various sample geometries for air–liquid interfaces, thin films, and solution and solid samples. The post-sample section consists of a 1 m WAXS section with two linear gas detectors, a vacuum bellows (1–4 m), a two-beamstop system and the SAXS detector system, all situated on a motorized optical bench for motion in six degrees of freedom. In particular, the vacuum bellows of a large inner diameter (260 mm) provides continuous changes of the sample-to-detector distance under vacuum. Synchronized SAXS and WAXS measurements are realized *via* a data-acquisition protocol that can integrate the two linear gas detectors for WAXS and the area detector for SAXS (gas type or Mar165 CCD); the protocol also incorporates sample changing and temperature control for programmable data collection. The performance of the instrument is illustrated *via* several different measurements, including (1) simultaneous SAXS/WAXS and differential scanning calorimetry for polymer crystallization, (2) structural evolution with a large ordering spacing of ~250 nm in a supramolecular complex, (3) SAXS for polymer blends under *in situ* drawing, (4) SAXS and anomalous SAXS for unilamellar lipid vesicles and metalloprotein solutions, (5) anomalous GISAXS for oriented membranes of Br-labeled lipids embedded with peptides, and (6) GISAXS for silicate films formed *in situ* at the air–water interface.

1. Introduction

Small-angle X-ray scattering (SAXS) is becoming increasingly popular in nanostructural characterization, as illustrated by the quickly multiplying number of SAXS beamlines in synchrotron radiation facilities worldwide. The state-of-the-art SAXS instruments fully functioning or under implementation at such synchrotron sources include, for example, beamlines SWING at Synchrotron SOLEIL (David & Pérez, 2009), ID2 at the ESRF (Narayanan *et al.*, 2001), X27C at the National Synchrotron Light Source at Brookhaven National Laboratory (Chu & Hsiao, 2001), non-crystalline diffraction I22 at the Diamond Light Source (http://www.diamond.ac.uk/Home/Beamlines/I22.html) and the small/wide-angle X-ray scattering beamline at the Australian Synchrotron (Kirby *et al.*, 2007). These examples demonstrate the flexibility and versatility of SAXS for a variety of measurements, such as combined SAXS and wide-angle X-ray scattering (WAXS) or

grazing-incidence SAXS (GISAXS). Because they have the unique feature of tunable beam energy, an increasing number of synchrotron-based SAXS instruments are capable of performing anomalous SAXS (ASAXS), such as beamlines 7T MPW SAXS at BESSY (http://www.helmholtz-berlin.de/forschung/funkma/werkstoffe/methoden/asaxs_en.html) and 15-ID-D ChemMatCARS at the Advanced Photon Source (Sutton *et al.*, 2004). Some extended ASAXS setups can accommodate complementary X-ray absorption measurements, for instance, the JUSIFA B1 ASAXS beamline at HASYLAB (Haubold *et al.*, 1997) and beamline 15A at the Photon Factory, KEK (Morita *et al.*, 2007). Furthermore, ultra-SAXS beamlines (Tsuruta *et al.*, 1998; Shinohara *et al.*, 2007; Ilavsky *et al.*, 2009) and SAXS beamlines with microbeams and/or coherent beams, *e.g.* beamline 40XU of the Super Photon ring-8 GeV (Inoue *et al.*, 2001), the microfocus beamline ID13 at the ESRF (Davies *et al.*, 2006) and the cSAXS beamline at the Swiss Light Source (Riekel, 2003), have broadened SAXS applications. Advances in small-angle scattering instruments for nano- to meso-structural studies have been recently reviewed by Allen (2005).

At beamline 23A of the National Synchrotron Radiation Research Center, Taiwan (NSRRC), which has a 1.5 GeV electron storage ring operated at a constant current mode of 300 mA (Wang *et al.*, 2006), we have newly installed a small/wide-angle X-ray scattering (SAXS/WAXS) instrument, with a superconducting wiggler source. This instrument incorporates many of the features mentioned above. In addition, with a special design of the deflectable beam, the instrument can perform GISAXS/GIWAXS at air–liquid/liquid–liquid interfaces, taking advantage of the available high-energy X-rays (up to 23 keV) in penetrating the top fluid phase for probing liquid–liquid interfaces. In this report, we describe features of this SAXS/WAXS instrument and illustrate its performance *via* several different measurements, including (1) simultaneous measurements with SAXS, WAXS and differential scanning calorimetry (DSC) for correlated changes of crystalline structures and nanostructures in polymer crystallization, (2) structural evolution over a large length scale of ∼250 nm in a supramolecular complex of a diblock copolymer grafted with amphiphilic mesogens, (3) SAXS for polymer blends under *in situ* drawing with a tensile stress tester, (4) SAXS and ASAXS for unilamellar lipid vesicles and metalloprotein solutions, (5) anomalous GISAXS for oriented membranes of Br-labeled phosphatidylcholine lipids embedded with peptides, and finally (6) GISAXS for surfactant-templated silicate films formed *in situ* at the air–water interface.

2. Instrument

2.1. X-ray source and beamline optics

The dedicated SAXS beamline 23A uses the X-ray source from the in-achromat superconducting wiggler insertion device of a constant magnetic field of 3.1 T. As details of the beamline have been described in a previous report (Liu *et al.*, 2009), here we only briefly outline the beamline optics and main features. The X-ray beam from the source is first collimated by a cylindrical mirror to decrease the vertical beam divergence by a factor of 10. With the two monochromators incorporated into one rotating cradle for fast exchange, the beam can be selectively monochromated by the double Si(111) crystal monochromator (DCM) for high energy resolution ($\Delta E/E \simeq 2 \times 10^{-4}$) in the energy range 5–23 keV, or by the double Mo/B_4C multilayer monochromator (DMM) for a 10–30 times higher flux of 2×10^{11} photons s^{-1} in the 6–15 keV range. Subsequently, the monochromated beam is focused by a toroidal mirror (FM) with 1:1 focusing for a small beam divergence and a beam size of *ca* 0.9 × 0.3 mm (horizontal × vertical) at the focus point located 26.5 m from the radiation source. Situated 5 m behind the FM is an Si-based plane mirror especially installed to selectively deflect the beam downwards for GISAXS with liquid surfaces/interfaces. Two online beam-position monitors located at 6 and 15 m from the radiation source provide an efficient feedback control mechanism to maintain the beam position within 20 μm stability.

2.2. Instrument layout

Located inside the BL23A experimental hutch (10 m in length and 4 m in width) is the SAXS/WAXS instrument composed of the collimation, sample and post-sample stages (Fig. 1). The collimation stage consists of a 10 ms beam shutter, two pinhole–slit systems, two beam-intensity monitors, two sets of attenuators, a laser alignment system and a rotary disc. The beam size is mainly defined by the first pinhole–slit system (P1) in the experimental hutch and the high-precision slits (S3) (in the beamline hutch) located 5 m before P1 (Liu *et al.*, 2009). The guard pinhole–slit system (P2) for eliminating parasitic scattering is connected to P1 *via* a bellows to allow an adjustable spacing of between 0.6 and 0.9 m, and can be translated to fit a variety of sample geometries for decreasing beam path in air.

The pinhole–slit systems P1 and P2 are modifications of the in-vacuum slits from JJ X-ray (Liseleje, Denmark), with two vertical tungsten carbide blades embedded (at 5 mm from the blade edge, 0.5 mm in thickness) with Ta pinholes of different sizes ranging from 0.2 to 1.0 mm in diameter. This modification allows a quick switch between the pinhole and slit beam collimation geometry for transmission SAXS or GISAXS. A diode laser (25 mW), passing through P1 and P2, provides rapid and convenient sample and beamstop preliminary alignments. There are two sets of attenuators, containing eight and nine attenuation channels, which are composed of Al, Cu or Bi foils of various thicknesses (72 possible combinations in total). This setup allows the beam intensity to be selectively attenuated in small increments or completely blocked, in order to deal with strongly scattering samples or for sample transmission measurements in a wide energy range of 5–23 keV. Sample transmission to X-rays is obtained by taking the ratio of the intensities of the highly attenuated direct beam measured with and without sample using the area detector. For sample transmission with low-energy X-rays (5–6 keV),

the beam intensity is decreased by closing the S3 (or P1) slits rather than using the metal-foil attenuators; this avoids the asymmetric (smaller) attenuation of the metal foils to the high harmonic X-rays of the primary beam, which otherwise would result in an enhanced high harmonic X-ray contribution in transmission measurements (Liu *et al.*, 2009) and hence an overestimated sample transmission coefficient. Beam intensity is monitored by two NaI scintillation counters located before and after P1; two 8 μm Mylar films are placed in the beam path as reflectors for the two beam monitors, which are also used in position alignment for S3 and P1. At the end of the collimation stage is a rotary disc, containing a photodiode detector for P2 alignment. Also on the rotary disc are nine standard metal foils for beam-energy calibration with X-ray absorption near-edge spectroscopy (XANES) as detailed below. All these components are situated on a 1 m-long motorized optical table, allowing motion in six degrees of freedom (6DoF); this mechanism provides synchronized tilting of the whole collimation system with the deflected beam in the case of GISAXS measurements for air–liquid interfaces, where several selected incident angles are usually needed.

Following the collimation stage is the 6DoF motorized sample stage for sample alignments, sample oscillation during measurements and sample changing. Vacuum-tight sample cells for solid and solution samples of various thicknesses between 1.2 and 5 mm are available for simultaneous SAXS/WAXS measurements; three-way-flow cells allow circulation of sample solutions or gas flow for solid samples during time-resolved SAXS/WAXS measurements. For protein solution SAXS, high-energy X-rays such as 14 keV are advantageous because of the lower X-ray absorption and hence decreased protein radiation damage. To further reduce radiation damage, protein solutions can be sealed with cells of large Kapton (or quartz) windows (5 mm in diameter) and rocked slowly and constantly within an area of 2 × 2 mm during data collection; this avoids prolonged spot exposure (generally 0.2–0.6 mm in beam diameter). Sample temperature is programmable *via* a silicon-oil-based cooler (NESLAB RTE-740 from Thermo Fisher Scientific Inc., Waltham, MA, USA) from 253 to 423 K or *via* heating rods of a faster heating rate from ∼303 to ∼673 K. A Mettler Toledo FP84 differential scanning calorimeter, a Linkam CSS450 shear stage, a Linkam TST350 tensile stress tester and a BioLOGIC SFM-400 four-syringe stopped-flow system have been modified for simultaneous SAXS/WAXS measurements.

The post-sample stage consists of the WAXS section, a vacuum bellows, a two-beamstop system and two area detectors, all situated on a 6DoF motorized optical table 7 × 4 × 1 m (length × width × height) in dimension, allowing for systematic alignment of the whole post-sample section with the X-ray beam. The post-sample vacuum piping starts with a 1 m pipe for WAXS, followed by a motorized vacuum bellows (260 mm inner diameter) capped by the beamstop chamber at the end. The 1 m pipe has two long slots (950 mm in length and 12 mm in width, sealed with 12 μm Kapton for vacuum) in the vertical and horizontal directions for WAXS. With these long slots, the two 20 cm linear detectors (gas type with the delay line readout system; Gabriel, 1977) can independently search for intermediate- to wide-angle X-ray scattering in the wavevector ($Q = 4\pi\lambda^{-1}\sin\theta$, where λ is the wavelength and 2θ the scattering angle) range of 0.3–4.0 Å^{-1}. The two-section vacuum bellows provides convenient and continuous changes in the sample-to-detector (SD) distance from 2.1 to 5.1 m (or 1.6 to 3.1 m, when only one section of the bellows is used), under vacuum; the bellows can be driven out of the beam path to further shorten the SD distance to 1.1 m. The large beamstop chamber (600 × 600 × 100 mm) accommodates two motorized Ta beamstops for wide-range translation in vacuum. Used for SAXS/GISAXS measurements, the first beamstop (of selectable size but usually 5 mm in diameter) can be translated in an area of 150 × 150 mm, covering most of the detecting field of the area detectors. The second beamstop is mainly used to block the direct beam in GISAXS measurements and can be completely translated out of the detector field in transmission-type SAXS measurements. A photodiode detector is attached to the GISAXS beamstop to collect sample-transmitted beam intensity; it can also be used in XANES measurements for samples or for standard foils in beam-energy calibration (the transmitted-beam intensity measured is normalized by the incident-beam intensity for sample X-ray absorbance). With this arrangement,

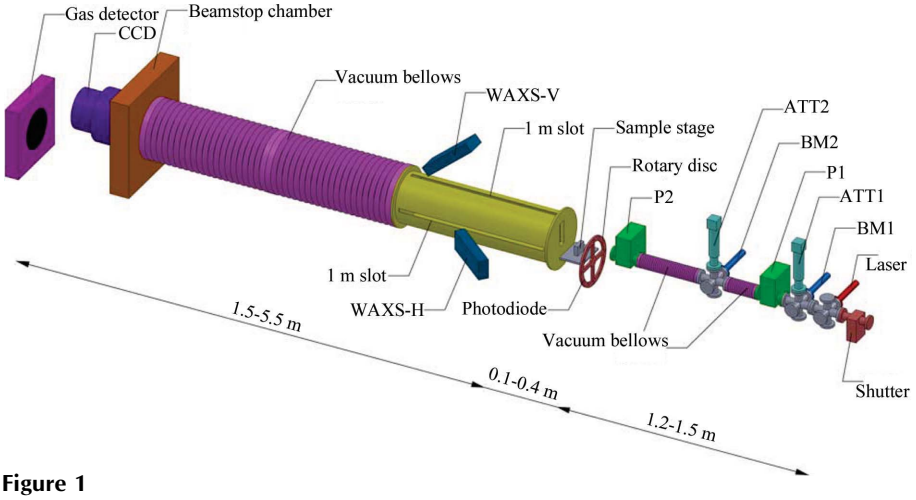

Figure 1
A schematic drawing of the BL23A SAXS/WAXS instrument. Starting from the right-hand side we show the collimation stage with the beam shutter, the laser alignment system, the two beam-intensity monitors (BM1 and BM2), the two sets of attenuators (ATT1 and ATT2), the pinhole–slit systems (P1 and P2), and the rotary disc containing a photodiode detector and nine standard metal foils for beam-energy calibration. The sample stage can accommodate a wide range of sample geometries. The post-sample stage includes subsequently (1) the 1 m WAXS section with WAXS-V and WAXS-H linear gas detectors for scanning WAXS along the two 1 m-long slots of the WAXS vacuum pipe, (2) the vacuum bellows, (3) the beamstop chamber and (4) the two interchangeable area detectors (a Mar165 CCD and a two-dimensional gas detector).

complementary XANES and anomalous SAXS/WAXS measurements can be performed for the same sample under the same sample environment.

Situated at the end of the post-sample section is the detector platform, docked with two area detectors: a Gabriel gas-type detector (D2L, Saint Cassien, France) with a detecting area of 200 × 200 mm and a Mar165 CCD detector (Mar USA Inc., Evanston, IL, USA) of an active area 165 mm in diameter. Readout systems of the area detectors are supplied by the respective manufacturers. On the detector platform, the motorized detector holders translate either of the two detectors into contact with the beamstop chamber. In the case of the gas detector, the detector body can directly seal (with an O-ring) the beamstop chamber and hence the post-sample vacuum, leaving the carbon window of the detector in vacuum. In the case of the CCD detector, the beamstop chamber is first sealed by a 75 µm Kapton window 170 mm in diameter before bringing in the CCD detector. The motorized detector platform, connecting the beamstop chamber that holds the bellows from the downstream side (Fig. 1), can translate (together with the SAXS detectors and the beamstop chamber) forward or backward to compress or stretch the vacuum bellows in order to change the SD distance under vacuum and thus the detectable Q region of the SAXS area detector. The 7 m optical table can swing the whole post-sample system by as much as 8° horizontally and 2° vertically. This mechanism provides a convenient beam-position offset up to 200 mm from the area-detector center for a wider Q range in one instrument geometry configuration, while keeping a fixed beam entrance position of the vacuum piping system. In calibrating the detector pixel sensitivity, offsetting the direct beam completely out of the area-detector field is necessary for fluorescence measurements with standard metal films (detailed below).

2.3. Data acquisition and instrument calibration

For simultaneous SAXS/WAXS measurements, the PC-based data-acquisition system for the SAXS detector (either Mar165 CCD or the gas detector) has been integrated with that for the two WAXS detectors based on a master–slave mode, where the SAXS system is the master and the WAXS system the slave. Under the master–slave mode, one-to-one correspondence between SAXS and WAXS data frames can be achieved, which is crucial in time-resolved measurements [details of the data-acquisition system for the gas detectors have been described by Shang *et al.* (2004)]. We have integrated the data-acquisition system in a protocol that further incorporates sample changing and temperature control for programmable data collection.

Calibration of the WAXS Q axis is carried out by a data-reduction algorithm developed from an analytical formula, which requires the input of three calibrated WAXS peaks of standard samples measured at the same sample position (Lai *et al.*, 2006). The same routine also corrects WAXS data for electronic noise, background scattering, angle-dependent sample path length and transmission, and incoming flux. The effects of detector pixel sensitivity, view angle and air-path-length-dependent absorption on the measured intensity are corrected simultaneously by dividing (pixel by pixel) the WAXS spectrum of the sample by the fluorescence spectrum of a metal sheet irradiated with the same

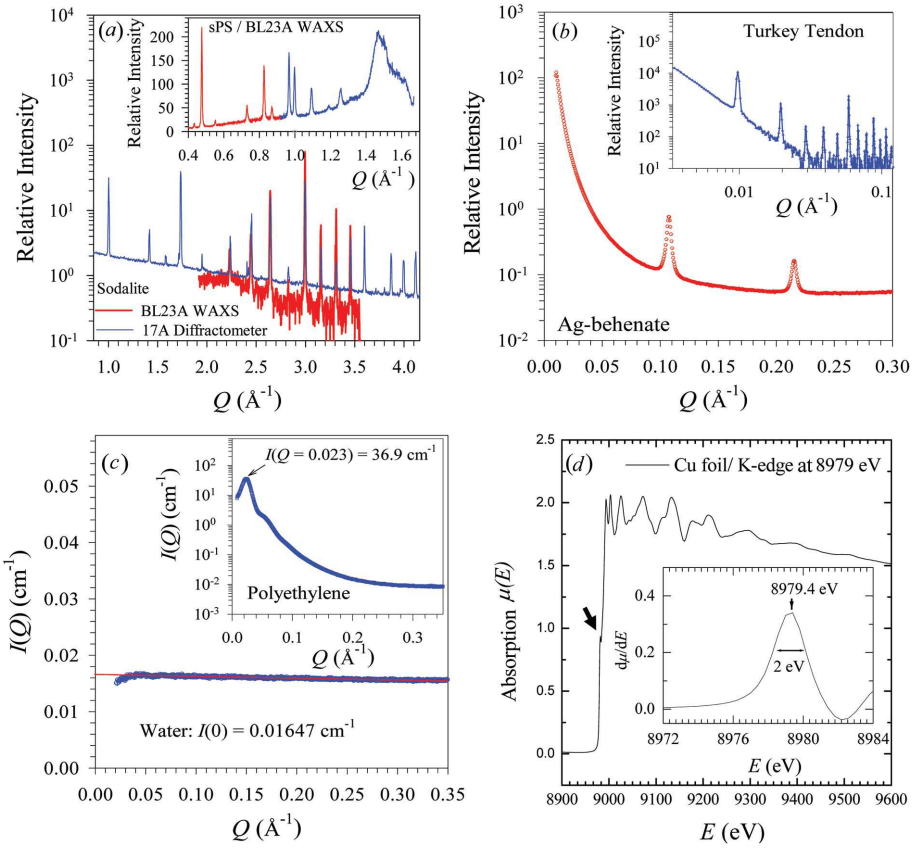

Figure 2
(*a*) Comparison of WAXS profiles of sodalite obtained, respectively, from the BL 23A SAXS/WAXS instrument (linear detector) and the BL17A diffractometer (imaging plate, without background-scattering subtraction). The inset shows the joint WAXS profiles collected simultaneously with the two linear detectors for the respective Q regions of 0.4–0.9 and 0.8–1.7 Å^{-1}. (*b*) Diffraction peaks of the standard samples silver behenate and turkey tendon (inset) are used in the SAXS Q calibration in the respective Q regions. (*c*) SAXS profiles of water and an HDPE sample (inset). The $I(0)$ value of water linearly extrapolated (solid line) from the data in the higher Q region (0.05–0.3 Å^{-1}) is reset to 0.01647 cm^{-1} for the absolute intensity. (*d*) X-ray absorption spectrum of a Cu foil measured with the BL23A SAXS/WAXS instrument, with the Cu pre-edge absorption indicated by an arrow. The inset shows the dμ/dE spectrum, with the peak position (indicated by an arrow) corresponding to the Cu K-edge absorption at 8979 eV and the peak width (2.0 eV) to the energy spread of the beam.

beam in the same detector configuration. Crystalline peaks of sodalite and syndiotactic polystyrene (sPS) covering a wide Q region of 0.4–4.0 Å^{-1} (Fig. 2*a*) are used in WAXS Q calibration. Fig. 2(*a*) shows the overlapping WAXS profiles of sodalite obtained by use of the BL23A SAXS/WAXS instrument and the well established diffractometer at BL17A, demonstrating the reliability of the new instrument for WAXS measurements. The inset of Fig. 2(*a*) illustrates the wide-Q-range WAXS profile of sPS, obtained with two linear detectors positioned for intermediate- and wide-angle X-ray scattering.

Silver behenate and turkey tendon with the first diffraction peaks located at Q = 0.1078 and 0.00985 Å^{-1}, respectively, are used for SAXS Q calibration in the high-Q and low-Q regions (Fig. 2*b*). Scattering from water or high-density polyethylene (HDPE) can be used as a secondary standard in placing SAXS profiles $I(Q)$ at the absolute scale defined as differential cross section per unit volume in units of cm^{-1} (Lai *et al.*, 2005, 2006). According to a previous study (Hendricks *et al.*, 1974), the theoretical value for the absolute scattering of water at $I(0)$ is 0.01647 cm^{-1} at temperatures ranging from 293 to 298 K. The scaling factor that brings the linearly extrapolated $I(0)$ value from the measured SAXS profile of water (Fig. 2*c*) to the theoretical value may then be applied to other SAXS profiles measured under the same instrument configuration to adjust them to the absolute scale. For instance, the SAXS profile of an HDPE sample (1.9 mm in thickness) thus calibrated has a peak intensity of 36.9 cm^{-1} at Q = 0.023 Å^{-1} (inset of Fig. 2*c*); thereafter, the high peak intensity of the HDPE sample (as compared to water scattering) can serve as a convenient secondary standard. The HDPE sample we used has isotropic scattering and a stable scattering profile (peak position and peak width) over years (Lai *et al.*, 2005, 2006); replacement with a fresh sample, however, is needed when the scattering profile can no longer be reproduced upon further extended ageing or radiation damage. The use of HDPE for SAXS intensity calibration has been reported previously by Wignall (1991).

A SAXS data-reduction routine has been developed to convert the two-dimensional scattering patterns collected with the area detectors into one-dimensional $I(Q)$ profiles. The SAXS data-reduction routine can efficiently process a batch of time-resolved SAXS images, and systematically correct all the data for detector electronic noise and pixel sensitivity, background scattering, sample transmission and thickness, and incident flux, then place the data on the calibrated Q axis and the absolute intensity scale. In the data-reduction routine, a premeasured two-dimensional fluorescence spectrum of a metal sheet irradiated with the same beam energy employed in sample measurements is used to correct the detector pixel sensitivity of the gas detector or Mar165 CCD, in a way similar to that described for WAXS data reduction. In the case of the CCD, it was found that inhomogeneity in the CCD pixel sensitivity is only a few percent for low-energy (5–6 keV) X-rays, and it is increasingly better for X-rays with increasingly higher energy (>10 keV). Presumably, higher-energy X-rays are relatively insensitive to small thickness variations in the phosphor layer of the CCD optimized for 10 keV X-ray detection. Based on this result, fluorescence spectra measured with X-rays in the energy range of 5–15 keV (in increments of 1 keV) are used in the pixel sensitivity calibration of the area detector; for SAXS data collected with X-rays in the range 16–23 keV, the two-dimensional fluorescence spectrum measured with 15 keV X-rays can be applied (for pixel sensitivity correction) in the SAXS data-reduction routine, without the loss of much accuracy.

For anomalous SAXS/WAXS or GISAXS/GIWAXS, the beam energy is calibrated by standard foils with XANES, as described previously. Fig. 2(*d*) illustrates the X-ray absorption spectrum measured for a standard Cu foil of the K-edge absorption at 8979 eV; the beam energy and energy spread

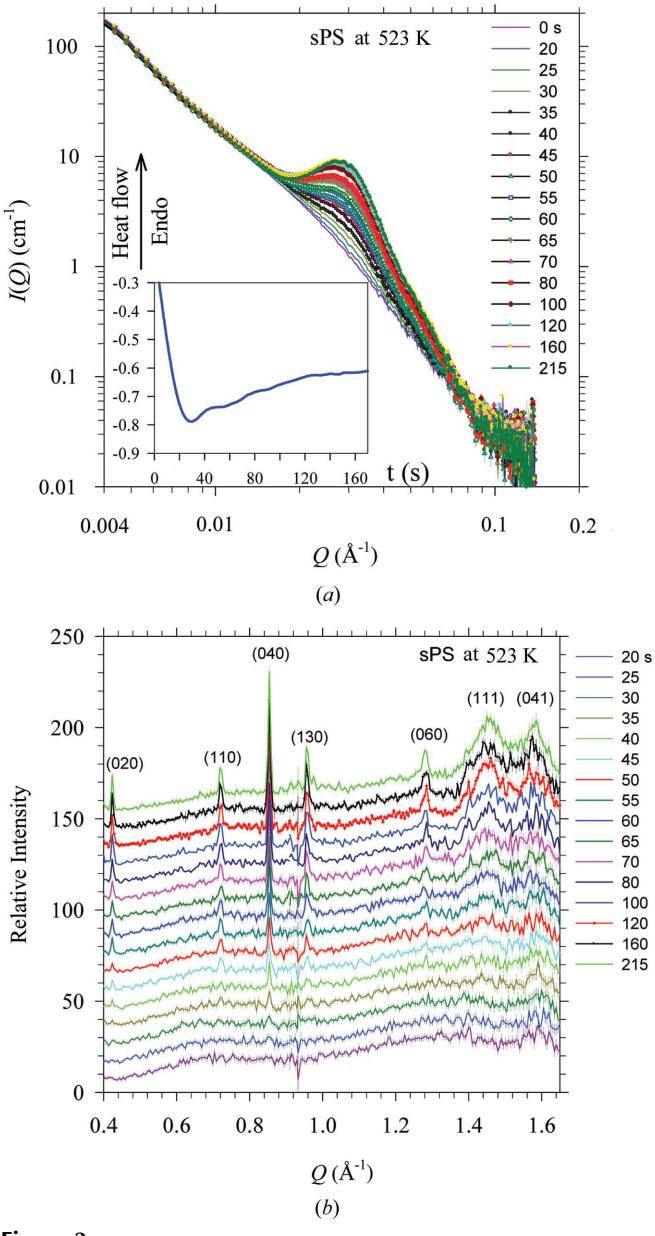

Figure 3
Time-resolved (*a*) SAXS and (*b*) WAXS profiles for the sPS specimen isothermally crystallized at 523 K, after quenching from the melt at 573 K. The inset in (*a*) shows the corresponding DSC trace.

(ΔE = 2 eV) are defined by the peak position and width in the energy-derivative spectrum shown in the inset.

3. Instrument performance

We have performed several measurements to illustrate the various aspects of the SAXS/WAXS instrument; unless specified, the SAXS data shown below were collected with the Mar165 CCD detector.

3.1. Small-, intermediate- and wide-angle X-ray scattering with DSC for polymer crystallization

Fig. 3 demonstrates the performance of the SAXS/WAXS instrument with simultaneous SAXS/WAXS/DSC. With a time resolution of 5 s, the measured SAXS and WAXS spectra concomitantly capture the evolution of nanostructure and crystalline structure of sPS (M_w = 140 kDa) isothermally crystallized at 523 K after quenching from the melt state at 573 K. The sPS specimen was placed in a Mettler Toledo FP84 DSC cell, modified with entrance/exit windows (2 and 7 mm in diameter, respectively) for the X-ray path (Su *et al.*, 2008). With a beam of 6 keV and SD distances of 2200 (SAXS), 960 (intermediate-angle X-ray scattering) and 500 mm (WAXS) for the area and the two linear detectors, respectively (Fig. 1), the SAXS and WAXS (combined spectra from the two linear detectors) profiles shown in Figs. 3(*a*) and 3(*b*) cover a wide Q range of 0.004–1.7 Å^{-1}. In the time-dependent SAXS profiles, a broad lamellar hump centered around Q = 0.028 Å^{-1} started to appear at $t \simeq$ 25–30 s after the initiation of isothermal crystallization; this was followed by the emergence of several crystalline peaks, including (020), (040) and (130) reflections in the WAXS spectrum at $t \simeq$ 40–45 s. The crystalline peaks developed quickly, together with the sharpening of the lamellar hump (in SAXS); both became asymptomatically saturated at $t \simeq$ 120 s. The corresponding DSC trace (inset of Fig. 3*a*) exhibited a dip around $t \simeq$ 20–40 s, coinciding with the onset of crystallization; it became eventless after $t \simeq$ 120 s where little structural change could be observed from the SAXS/WAXS spectra. The SAXS/WAXS/DSC results simultaneously collected over a single sample provide excellent correlations between the development of nano/crystalline structures and the observed thermal events in this particular case of sPS melt crystallization.

3.2. High flux and fast data collection for the kinetics of polymer crystallization

To capture rapid nanostructural changes with SAXS, both high X-ray flux and fast data collection are indispensable. With the frame-shift mode of the Mar165 CCD for sub-second data collection, it is possible to capture structural evolution details in the early stage of polymer crystallization with the new SAXS instrument of 2×10^{11} photons s^{-1} under DMM mode. In the frame-shift imaging mode, a 170 mm-long slit of variable opening was mounted in front of the CCD detector to allow down-sizing of the CCD exposure area. The mask creates a fast storage area on the CCD chip such that, after each exposure of the unmasked area, the CCD can be triggered to quickly shift the image to the masked region. With a slit opening S, the CCD can continuously take n = 165 mm S^{-1} exposures and then dump all the accumulated rectangular frame images at one time; this significantly reduces the measurement deadtime caused by data dumping (typically 2.5–3.5 s is required for dumping a full image of 165 mm diameter, but relocating the frame-shift images on the CCD chip requires only some tens of milliseconds, depending on the size of the exposure area and settings). The imaging speed (and hence the exposure time of each frame) can be controlled by external trigger signals (*e.g.* transistor–transistor logic pulses from a function generator).

Fig. 4(*a*) displays seven continuous SAXS images taken for a chicken tendon at an imaging speed of 10 Hz (100 ms cycle time per frame, including 44 ms exposure time and 56 ms shift

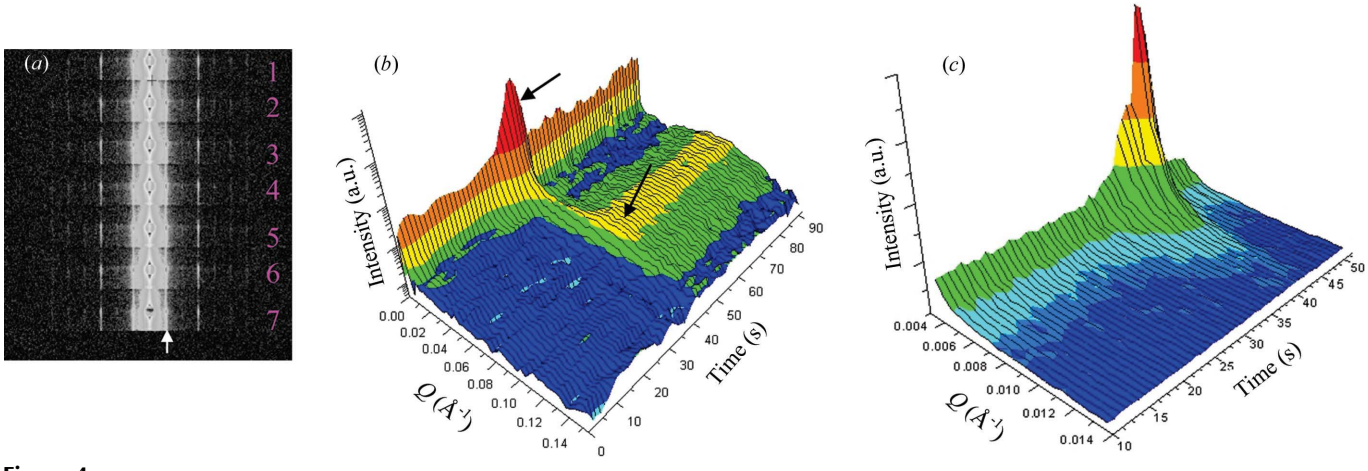

Figure 4
(*a*) Seven continuous SAXS frame images (100 ms cycle time per frame) taken for a chicken tendon. The arrow indicates the first diffraction peak at Q = 0.00946 Å^{-1}. (*b*) SAXS profiles of a PTT sample taken during cold crystallization at 341 K using a frame-shift imaging rate of 2 Hz. The arrows mark the low-Q transient scattering and the development of ordered structure in the high-Q region, respectively. (*c*) A zoom-in view (in both Q and time axes) to emphasize the low-Q transient scattering about 40 s in to the cold crystallization process.

time), using a 7 keV beam and an SD distance of 3250 mm. The first diffraction peak at Q = 0.00946 Å^{-1} (which corresponds to the characteristic spacing of 664 Å) and several of its high-order satellites are clearly discernible. With the same SAXS instrument configuration but a slower imaging rate of 2 Hz (*i.e.* setting the CCD to continuously take eight frame images for 4 s with a time resolution of 0.5 s before data dumping), we have applied frame-shift imaging to the kinetics of polymer crystallization. Shown in Figs. 4(*b*) and 4(*c*) are SAXS profiles converted from the SAXS images of semi-rigid poly(trimethylene terephthalate) (PTT, melting temperature T_m = 503 K and glass transition temperature T_g = 318 K) cold crystallized at 341 K after quenching in ice–water from the melt state. These profiles capture a transient scattering in the low-Q region 0.004–0.008 Å^{-1} at $t \simeq 40$ s into the cold crystallization process. The transient structure subsided quickly within a few seconds, with concomitant emergence of scattering centered at Q = 0.065 Å^{-1} (*i.e.* ∼10 nm in characteristic length scale). The transient scattering could be delayed by lowering of the cold crystallization temperature. It appears that the transient scattering in the low-Q region may be associated with thermally driven density fluctuations or some sort of gelation process of polymer chains, on a length scale much greater than the characteristic domain spacing of typically ∼10 nm, prior to the formation of crystalline domains.

3.3. Resolving large ordering spacing

The spatial resolving power of the SAXS/WAXS instrument critically depends on the minimum Q value available. Fig. 5 demonstrates such a test of the instrument Q minimum using a supramolecular complex comprising a highly asymmetric block copolymer polystyrene-*block*-poly(4-vinylpyridine) (PS_{5356}-*b*-$P4VP_{714}$) with the volume fraction of the PS block $\varphi_{PS} \simeq 0.88$; the P4VP blocks are grafted with amphiphilic 4′-(3,4,5-tridodecyloxybenzoyloxy)benzoic acid molecules (TDB) (binding ratio $\simeq 0.7$) for a side-chain liquid crystal (LC) phase (Chuang *et al.*, 2009). The temperature-dependent SAXS profiles (Fig. 5), measured with a 6 keV (λ = 2.067 Å) beam 0.2 mm in diameter and an SD distance of 5 m, exhibit a clear shift of the first lamellar peak in the very low Q region, from Q = 0.0028 Å^{-1} at 298 K to 0.0022 Å^{-1} at 463 K in the heating process. The peak shifting corresponds to an increase in the lamellar spacing from 220 to 285 nm. The length change on such a large scale correlates well to the observed color shifting of this photonic oriented complex from blue to light blue upon heating. It is likely that dissociation of the LC phase of TDB in the supramolecular complex during heating may be responsible for the increase in lamellar spacing. Simultaneous SAXS/WAXS studies in the near future might be helpful in clarifying this point, as evolution of the liquid crystal phase of TDB (in the WAXS regime) can be observed concomitantly.

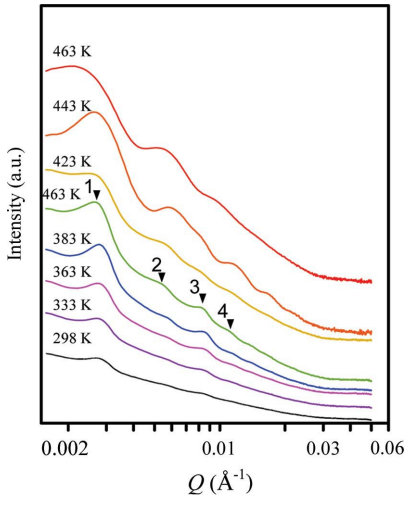

Figure 5
Temperature-dependent SAXS profiles (intensity rescaled for clarity) of a supramolecular complex of PS-*b*-P4VP/TDB from 298 K (bottom curve) to 463 K (top curve), with selected lamellar peaks indexed.

3.4. *In situ* SAXS for polymer films under tensile elongation

To perform SAXS/WAXS with polymer films under *in situ* drawing at a specific annealing temperature, we have modified a tensile stress tester, Linkam TST350, with a 2 mm-diameter entrance and a larger exit angle of 42.5°. A blend film of poly(butylene adipate) (PBA, M_w = 12 kDa) and poly(vinyl chloride) (PVC, M_w = 106 kDa), 6/4 *w*/*w* in composition, 6 × 20 mm in area and 0.3 mm in thickness, was solution-cast from tetrahydrofuran and annealed in the tensile tester at 363 K under an extension ratio Λ = 2. This annealing temperature was above the T_m of PBA but below that of PVC. Therefore, after quenching to 278 K under constant stress, the film strength could be reinforced by the recrystallization of stress-aligned PBA crystals. The stress was released after PBA crystallization and the film was re-stretched to a series of extension ratios ranging from Λ = 1 to 3 at ambient temperature (∼300 K) for simultaneous SAXS/stress–strain measurements. Demonstrated in Fig. 6(*a*) is the stress–strain curve, with the *in situ* two-dimensional SAXS images given as insets. The corresponding SAXS profiles in Fig. 6(*b*) indicate that the deterioration of the PBA lamellar peak around $Q_x \simeq$ 0.058 Å^{-1} for $\Lambda > 1.5$ is closely related to the drawing of the film. In contrast, PVC crystals are increasingly better aligned upon elongation, resulting in sharpening of the lamellar peak; the peak shifts from 0.018 (d = 350 Å at Λ = 1) to 0.006 Å^{-1} (d = 1050 Å at Λ = 3), showing a threefold increase in the inter-grain spacing of PVC crystals that coincides with the macroscopic extension ratio of 3. These observations suggest that, after rupture of the stress-aligned PBA crystals, PVC lamellae remain largely intact, under the increasingly larger elongation.

3.5. Solution SAXS and ASAXS for proteins and lipid vesicles

During the past decade, protein solution SAXS has attracted considerable attention owing partly to advances in X-ray instrumentation/sources and partly to progress in data analysis algorithms for building low-resolution structural models of proteins from X-ray solution scattering data (Koch *et al.*, 2003). As the majority of proteins aggregate easily, the concentration of protein solutions for SAXS is usually kept

low (typically a few mg ml^{-1}), resulting in weak scattering especially in the higher-Q region (>0.1 Å^{-1}). In addition, radiation damage limits the X-ray exposure time for protein solution studies. These difficulties are partly alleviated by adopting synchrotron-based SAXS. The BL23A SAXS/WAXS instrument can provide a high-energy beam (*e.g.* 14 keV) to reduce X-ray absorption. In addition, a wide X-ray energy range (5–23 keV) is available for ASAXS which has been shown to be particularly useful in revealing the composition and/or distribution of heavy atoms (ions) enclosed in metalloproteins or lipid membranes (Li *et al.*, 2009; Bota *et al.*, 2007).

Shown in Fig. 7 is the result of an ASAXS application of the BL23A SAXS/WAXS instrument to a ferritin solution of 5 mg ml^{-1}. Ferritin consists of a spherical protein shell composed of 24 subunits (of inner and outer diameters of *ca* 40 and 60 Å, respectively) and an Fe core of several thousand ions (Harrison & Arosio, 1996). As the X-ray energy changed from 8 keV to the Fe K-edge absorption 7.112 keV (with the energy calibrated by an Fe sheet; *cf.* Fig. 2*d*), the measured ASAXS profile drops significantly in intensity compared with that measured at 8 keV, because of the substantial Fe content in the protein. Moreover, the intensity drops by 25 and 35% in the low-Q (0.01–0.05 Å^{-1}) and high-Q regions (0.1–0.3 Å^{-1}), respectively; this asymmetric decrease in intensity indicates an inhomogeneous distribution of Fe ions in the protein. The larger intensity decrease in the high-Q region dominated by the core implies a higher Fe ion concentration in the core region (~4 nm) of the protein (Sheu *et al.*, 2008; Jeng *et al.*, 2007), whereas the 25% intensity decrease in the low-Q region corresponds to the overall Fe content (~4600 Fe ions) in the protein. ASAXS has also been used to reveal the Fe core structure of ferritin (Stuhrmann, 1980) *via* the energy-sensitive radius of gyration R_g. In principle, the decrease in the forward (zero-angle) scattering intensity $I(0)$ depends on the ratio of the scattering intensity of the Fe ions with respect to that of the whole ferritin molecule (Li *et al.*, 2009). Also shown in Fig. 7, for comparison purposes, are the SAXS profiles obtained for the apoferritin (ferritin depleted of Fe ions) solution with the same instrumental conditions as those used for the ferritin solution. The well overlapped SAXS profiles of the apoferritin solution are essentially independent of the X-ray energy, ensuring reliability of the ASAXS measurements.

Interactions of biomolecules with membranes and the consequent structural changes are of great interest in life science. Lipid bilayers in the form of multilamellar vesicles or oriented multibilayers in a fully hydrated state are often

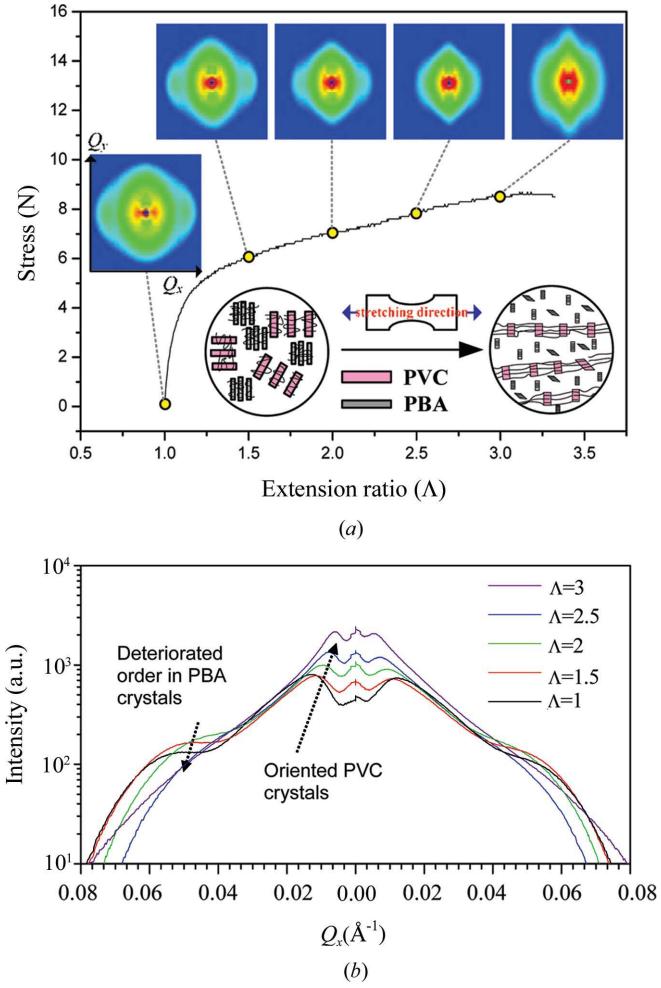

Figure 6
(*a*) The stress–strain curve for a PVC/PBA blend film, with *in situ* determined SAXS patterns (inset) at SD = 3169 mm and E = 8 keV. Cartoons illustrate the disruption of PBA lamellae upon stretching whereas the crystalline order in PVC lamellae increases with increasing strain. (*b*) The corresponding SAXS profiles taken from the two-dimensional images along the stretching direction. Arrows indicate that, for Λ > 1.5, the PBA lamellar peak gradually diminishes whereas the PVC lamellar peak sharpens and shifts to the low-Q region.

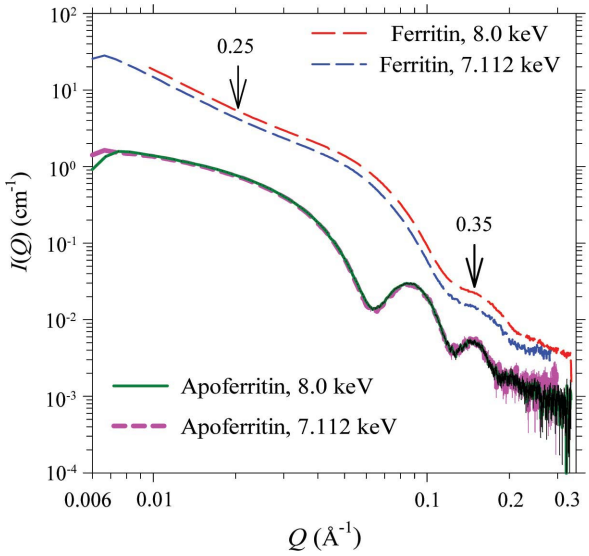

Figure 7
Anomalous SAXS profiles for the ferritin and apoferritin solutions (5 mg ml^{-1}) measured, respectively, at 8 and 7.112 keV (iron K-edge absorption). Arrows indicate Q regions where the intensity drops by 25 and 35%, respectively, when the beam energy is changed from 8 to 7.112 keV. In contrast, the similarly obtained SAXS profiles for the iron-free apoferritin solution overlap well.

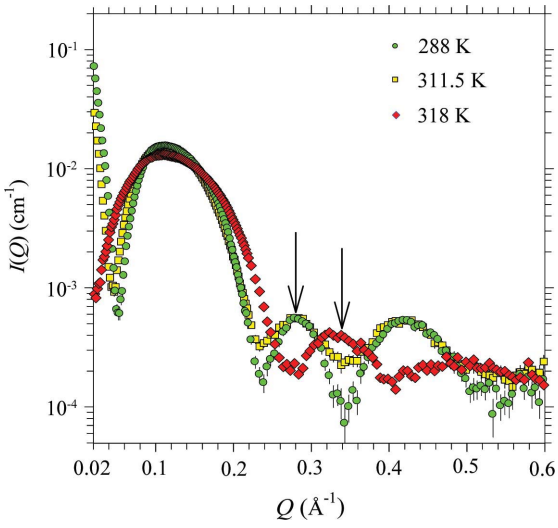

Figure 8
Temperature-dependent SAXS profiles for an aqueous solution of 10 m*M* DPPC unilamellar vesicles. The peak position of the second hump shifts from 0.28 Å^{-1} at 288 K (gel phase) to 0.33 Å^{-1} at 318 K (LC phase), as indicated by the arrows.

adopted as mimic membranes in understanding phenomena such as membrane thinning/thickening upon peptide binding. Structural changes in the bilayer spacing of several nanometres have often been probed *via* SAXS. Displayed in Fig. 8 are the temperature-dependent SAXS profiles (determined with SD = 1270 mm and E = 14 keV) for an aqueous 10 m*M* solution of dipalmitoylphosphatidylcholine (DPPC) in the form of unilamellar vesicles. Scattering intensity as low as 10^{-4} cm^{-1} can still be differentiated with the SAXS/WAXS instrument (note that water has a scattering intensity of 10^{-2} cm^{-1}; *cf.* Fig. 2*c*). At this resolution level, we were able to observe a significant peak shift of the second-order hump for the unilamellar vesicles when the temperature was increased from 288 to 318 K (Fig. 8); this shift from Q_{002} = 0.28 to 0.33 Å^{-1} is directly associated with the change of the head-to-head thickness, d_L, of the single lipid bilayer in the gel-to-LC phase transition. From the peak positions, we have estimated the change of d_L (= $4\pi/Q_{002}$) (Engelman, 1971) as from 44.7 Å at 288 K (the gel phase) to 38.5 Å at 318 K (the LC phase). Such a change coincides remarkably well with that observed previously in multilamellar DPPC bilayers (Nagle & Nagle, 2000). At 311.5 K, however, there was no observable peak position shift that could be related to the ripple phase structure of multilamellar vesicles. It appears that the ripple structure requires support from confining neighbor bilayers, and hence is limited to multilamellar vesicles/membranes (Nagle & Nagle, 2000; Jeng, Hsu, Lin *et al.*, 2005). With the instrumental resolution here, it is straightforward to extend this methodology to systems containing unilamellar lipid vesicles embedded with peptides to follow *in situ* membrane thinning/thickening upon peptide binding routes from the changes in the Q_{002} peak position directly.

3.6. GISAXS and anomalous GISAXS (AGISAXS)

Oriented thin films on a solid substrate often manifest rich structural features that critically influence the related device performance. To probe the structural characteristics of such sample thin films, it is necessary to perform SAXS in grazing-incidence geometry (Als-Nielsen *et al.*, 1994; Jeng, Hsu, Sun *et al.*, 2005; Haubold *et al.*, 1997). With a typical incidence angle $\theta_{in} \simeq 0.2^\circ$ (for 8 keV X-rays) for a glass substrate or silicon wafer and a sample size L = 30 mm along the incident beam, the effective beam size (that can be fully intercepted by the sample) is therefore $L \sin\theta_{in} \simeq 100$ µm in the vertical direction. Being equipped with the pinhole–slit collimation system for a flexible choice of beam size and the two independent beamstops for blocking the direct beam and the specular beam from the substrate (as detailed in §2.2), the BL23 SAXS/WAXS instrument can be easily converted to the GISAXS mode from the transmission SAXS mode. A GISAXS sample-alignment routine has been developed for systematic alignments of sample surfaces to the incident beam with a selected incident angle. The GISAXS Q axis is calibrated with the diffraction peaks of a silver behenate thin film coated on an Si substrate. Shown in Fig. 9(*b*) are the GISAXS profiles of the silver behenate thin film measured with six successive changes in beam energy from 13.157 to 13.459 keV at θ_{in} = 0.3° and SD = 1230 mm. The use of a high incident angle substantially above the critical angle of the Si substrate (0.14° at 13 keV) largely eliminates the reflected beam and the associated scattering, resulting in easier GISAXS Q calibration (Jeng, Hsu, Sun *et al.*, 2005; Lee *et al.*, 2006). On the other

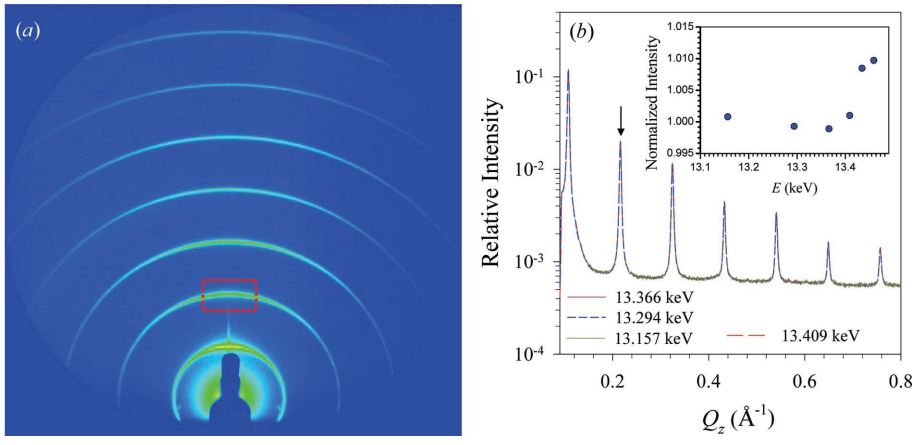

Figure 9
(*a*) Two-dimensional GISAXS pattern of a thin film of silver behenate on an Si substrate, measured with the 13.157 keV beam at θ_{in} = 0.3° and SD = 1230 mm. (*b*) Four representative GISAXS profiles taken along the meridian of the two-dimensional images measured with the corresponding beam energy indicated. Shown in the inset are the small intensity variations within ±0.5% of the second lamellar peak (indicated by an arrow) upon six successive beam-energy changes from 13.157 to 13.459 keV, with no need for beam-position realignment.

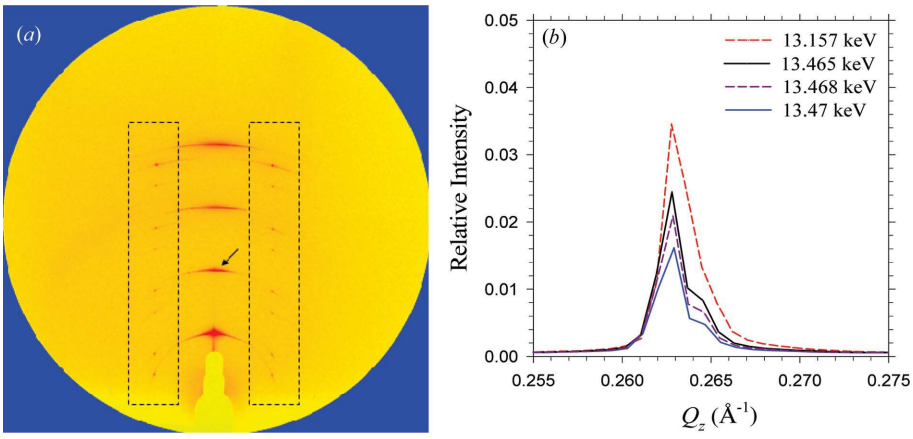

Figure 10
(*a*) Anomalous GISAXS image taken at 13.470 keV for an oriented membrane of Br-labeled DOPC embedded with melittin. The boxed regions highlight the characteristic reflections of the peptide–lipid pore phase structure. (*b*) Representative intensity profiles of the second-order lamellar peak [indicated by the arrow in (*a*)] along the meridian of the two-dimensional GISAXS patterns obtained with increasing beam energy from 13.157 to 13.47 keV.

hand, the well overlapped GISAXS profiles shown in Fig. 9(*b*) ensure measurement stability with changing beam energy (inset of Fig. 9*b*), which is essential in anomalous GISAXS measurements with an emphasis on quantitative analysis (Li *et al.*, 2009).

Recently, a sophisticated methodology with anomalous GISAXS has been developed to resolve the pore phase structure of peptide–lipid mixtures; energy scans near (and below) the absorption edge of the labeling atoms of the lipids were used to reveal the phase information of the small-angle diffractions from the mixture *via* the intensity changes of the diffraction peaks with beam energy (Qian *et al.*, 2008). Fig. 10(*a*) displays a GISAXS pattern from such a membrane of Br-labeled dioleoylphosphatidylcholine (DOPC), 1,2-di-(9,10-dibromo)stearoyl-*sn-glycero*-3-phosphocholine, embedded with the peptide melittin, under 45% relative humidity. With decreasing humidity from 94 to 45% at 303 K, the lamellar peaks shift toward the higher-Q region, signifying shrinkage of the bilayer spacing owing to loss of water. Concomitantly, two sets of satellite diffraction peaks sitting by the meridian lamellar peaks gradually appear and intensify. The final GISAXS pattern (Fig. 10*a*) corresponds to a three-dimensional ordered pore structure (Qian *et al.*, 2008). Selectively shown in Fig. 10(*b*) are the energy-dependent second lamellar peak profiles, manifesting a systematic intensity decrease with increasing beam energy from 13.157 to 13.470 keV (4 eV below the *K*-edge absorption of Br). From the observed intensity changes, the phase of the diffraction peak can be determined. With the phase information of all the diffraction peaks retrieved, it is possible to reconstruct the electron-density distribution of the unit cell of the pore phase and hence the pore structure of the DOPC/melittin complex (Pan *et al.*, 2006).

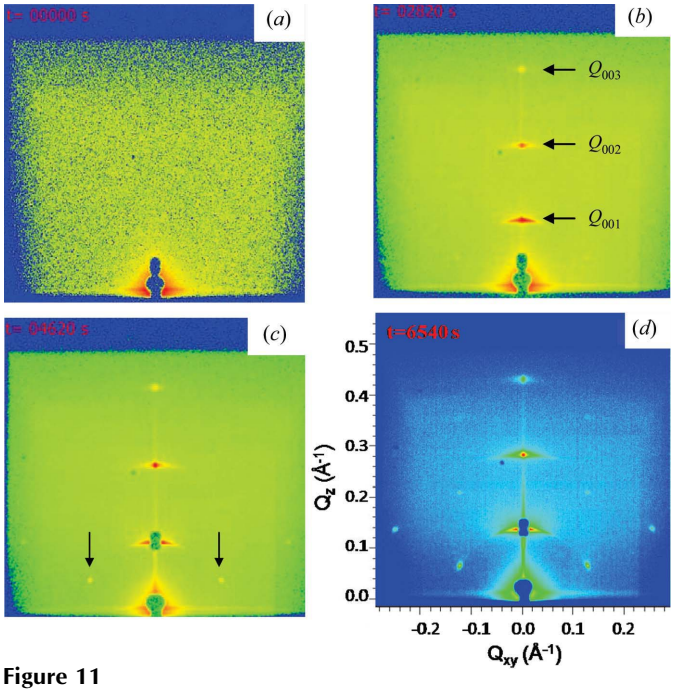

Figure 11
Representative GISAXS images taken with the two-dimensional gas detector at (*a*) 0 s, (*b*) 2820 s, (*c*) 4620 s and (*d*) 6540 s, for the formation process of a highly ordered CATB–silicate film at the air–water interface. Arrows in (*b*) and (*c*) indicate, respectively, the three lamellar reflections (Q_{001} = 0.14 Å^{-1}) and the two reflections from a hexagonal phase. (*d*) Single-crystal-like reflections indicate a hexagonally packed structure for the free-standing CTAB–silicate film.

3.7. *In situ* GISAXS from the air–water interface

The air–water interface connects two highly unsymmetrical environments, which is advantageous in orientating amphiphilic molecules to form highly ordered films of small surface roughness (Yang *et al.*, 1996). Probing in-plane as well as normal-to-plane structures of such films grown on a gravity-levelled air–water interface of atomic smoothness, however, requires a deflectable beam for a selectable incident angle. With an Si-based plane mirror installed at the BL23A SAXS/WAXS beamline, the beam incident angle on the water surface can be freely tuned close to the critical angle for total reflection (Liu *et al.*, 2009) for improved sensitivity to nanostructures at/near the air–water interface. We demonstrate below such a GISAXS application for the growth of a surfactant-templated silicate film formed *in situ* at the air–water interface.

The sample solution was prepared by adding tetraethyl orthosilicate (TEOS) to a surfactant solution of cetyltrimethylammonium bromide (CTAB) of pH < 1, with molar composition H_2O:HCl:CTAB:TEOS = 100:2:0.11:0.7. The mixture was poured into a Teflon trough, 100 × 100 mm in area and 0.7 mm in depth, which was inserted into an Al box

with Kapton windows for GISAXS at ambient temperature (298 K). GISAXS images (Fig. 11) were collected with an imaging rate of 2 frames min^{-1}, using a 10 keV beam and a grazing-incidence angle of 0.15°. Within the first 1200 s, the GISAXS patterns were relatively featureless (Fig. 11*a*). At the end of this induction stage, the first faint lamellar peak appeared, followed by the emergence of second- and third-order lamellar peaks. These peaks, signifying the formation of lamellae at the air–water interface, intensified with time and became eminent around $t = 2820$ s (Fig. 11*b*). At $t = 4620$ s, two side peaks by the meridian lamellar peaks were clearly observable (Fig. 11*c*), implying a transition of the layer structure to a hexagonal structure in the surface film. Presumably, the polymerization of TEOS initiated an in-plane rearrangement of the three-dimensional ordered structure. The GISAXS image taken at the end of the 2 h observation exhibits single-crystal-like reflections (Fig. 11*d*), indicating a surface film with a highly ordered structure of hexagonal packing. The detailed formation process thus recorded greatly facilitates the understanding of the formation mechanism of the CTAB–silicate film at the air–water interface.

It would not be difficult to extend the study of the air–water interface to liquid–liquid interfaces with the SAXS/WAXS instrument, as there are high-energy X-rays available up to 23 keV for adequate penetration of the beam through the top fluid phase. For instance, with a beam of 22 keV and an incident angle of 0.15°, the beam can penetrate a thick hexane film (with an X-ray path length of up to 25 mm) on top of a water substrate and reach the hexane–water interface with >75% residual beam intensity.

4. Concluding remarks

With the performance illustrated in this paper, the BL23A SAXS/WAXS instrument at NSRRC proves to be versatile for a wide range of applications in the structural characterization of soft matter and nanomaterials, covering a length scale from 0.1 to 300 nm and a time resolution down to 100 ms. The tunable beam energy from 5 to 23 keV renders anomalous SAXS and GISAXS feasible for multiphase/hierarchical systems containing various heavy atoms such as core–shell bimetallic nanoparticles and semiconductor quantum dots, metalloproteins, and metal-labeled lipid/peptide complexes. In particular, the deflectable beam design allows for GISAXS characterization of air–liquid/liquid–liquid interfaces. Measurements are greatly facilitated by the ease of, and stability in, beam energy change as well as the fast switch between the two monochromators of DCM and DMM for either high energy resolution or high flux. The large vacuum bellows provides convenient and continuous changes in the sample-to-detector distance under vacuum. The rigorous and efficient data-reduction routines provide support to the processing of a large quantity of SAXS/WAXS data collected from time-resolved measurements. Currently, the instrument is being used for a variety of projects including ongoing studies for the systems mentioned above.

We gratefully acknowledge support from the beamline group (in construction of the endstation) and the accelerator operation group (in the installation/operation of the beam position feedback control system) at NSRRC. We thank Dr H. Tsuruta and Professor T.-L. Lin for helpful discussions and suggestions for the endstation design. Thanks are also due to Mr R. Doyle for help with the setup and operation of the Mar165 CCD, to Dr H. Masunaga for help with the design of the beamstop chamber, and to Mr W. Y. Peng and Ms M. Li for help with the preparation of specimens. Proofreading by Professor A. C. Su is greatly appreciated.

References

Allen, A. J. (2005). *J. Am. Ceram. Soc.* **88**, 1367–1381.
Als-Nielsen, J., Jacquemain, D., Kjaer, K., Leveiller, F., Lahav, M. & Leiserowitz, L. (1994). *Phys. Rep.* **246**, 251–313.
Bota, A., Varga, Z. & Goerigk, G. (2007). *J. Phys. Chem. B*, **111**, 1911–1915.
Chu, B. & Hsiao, B. (2001). *Chem. Rev.* **101**, 1727–1761.
Chuang, W.-T., Sheu, H.-S., Jeng, U., Wu, H.-H., Hong, P.-D. & Lee, J.-J. (2009). *Chem. Mater.* **21**, 975–978.
David, G. & Pérez, J. (2009). *J. Appl. Cryst.* **42**, 892–900.
Davies, R. J., Burghammer, M. & Riekel, C. (2006). *Synchrotron Rad. Nat. Sci.* **5**, 1–2.
Engelman, D. M. (1971). *J. Mol. Biol.* **58**, 153–165.
Gabriel, A. (1977). *Rev. Sci. Instrum.* **48**, 1303–1305.
Harrison, P. M. & Arosio, P. (1996). *Biochim. Biophys. Acta*, **1275**, 161–203.
Haubold, H.-G., Wang, X. H., Goerigk, G. & Schilling, W. (1997). *J. Appl. Cryst.* **30**, 653–658.
Hendricks, R. W., Mardon, P. G. & Shaffer, L. B. (1974). *J. Chem. Phys.* **61**, 319–322.
Ilavsky, J., Jemian, P. R., Allen, A. J., Zhang, F., Levine, L. E. & Long, G. G. (2009). *J. Appl. Cryst.* **42**, 469–479.
Inoue, K., Oka, T., Suzuki, T., Yagi, N., Takeshita, K., Goto, S. & Ishikawa, T. (2001). *Nucl. Instrum. Methods Phys. Res. Sect. A*, **467**, 674–677.
Jeng, U., Hsu, C.-H., Lin, T.-L., Wu, C.-M., Chen, H.-L., Tai, L.-A. & Hwang, K.-C. (2005). *Physica B*, **357**, 193–198.
Jeng, U., Hsu, C.-H., Sun, Y.-S., Lai, Y.-H., Chung, W.-T., Sheu, H.-S., Lee, H.-Y., Song, Y.-F. & Liang, K. S. (2005). *Macromol. Res.* **13**, 506–513.
Jeng, U.-S., Lai, Y.-H., Sheu, H.-S., Lee, J.-F., Sun, Y.-S., Chuang, W.-T., Huang, Y.-S. & Liu, D.-G. (2007). *J. Appl. Cryst.* **40**, s418–s422.
Kirby, N., Boldeman, J. W., Gentle, I. & Cookson, D. (2007). *AIP Conf. Proc.* **879**, 887–889.
Koch, M. H. J., Vachette, P. & Svergun, D. I. (2003). *Q. Rev. Biophys.* **36**, 147–227.
Lai, Y.-H., Sun, Y.-S., Jeng, U.-S., Lin, J.-M., Lin, T.-L., Sheu, H.-S., Chuang, W.-T., Huang, Y.-S., Hsu, C.-H., Lee, M.-T., Lee, H.-Y., Liang, K. S., Gabriel, A. & Koch, M. H. J. (2006). *J. Appl. Cryst.* **39**, 871–877.
Lai, Y. H., Sun, Y. S., Jeng, U., Song, Y. F., Tsang, K. L. & Liang, K. S. (2005). *Nucl. Instrum. Methods Phys. Res. Sect. B*, **238**, 205–213.
Lee, B., Lo, C.-T., Seifert, S. & Winans, R. E. (2006). *J. Appl. Cryst.* **39**, 749–751.
Li, M., Huang, Y.-S., Jeng, U., Hsu, I.-J., Wu, Y. S., Lai, Y.-H., Su, C.-H., Lee, J.-F., Wang, Y. & Chang, C.-C. (2009). *Biophys. J.* **97**, 609–617.
Liu, D.-G. *et al.* (2009). *J. Synchrotron Rad.* **16**, 97–104.
Morita, T., Tanaka, Y., Ito, K., Takahashi, Y. & Nishikawa, K. (2007). *J. Appl. Cryst.* **40**, 791–795.

Nagle, J. F. & Nagle, S. T. (2000). *Biochim. Biophys. Acta*, **1469**, 159–195.
Narayanan, T., Diat, O. & Boesecke, P. B. (2001). *Nucl. Instrum. Methods Phys. Res. Sect. A*, **467–468**, 1005–1009.
Pan, D., Wang, W., Liu, W., Yang, L. & Huang, H. W. (2006). *J. Am. Chem. Soc.* **128**, 3800–3807.
Qian, S., Wang, W., Yang, L. & Huang, H. W. (2008). *Proc. Natl Acad. Sci. USA*, **105**, 17379–17383.
Riekel, C. (2003). *Nucl. Instrum. Methods Phys. Res. Sect. B*, **199**, 106–111.
Shang, W., Robrahn, B., Golding, F. & Koch, M. H. J. (2004). *Nucl. Instrum. Methods Phys. Res. Sect. A*, **530**, 513–520.
Sheu, H.-S., Jeng, U., Shih, W.-J., Lai, Y.-H., Su, C.-H., Lai, C.-W., Yang, M.-J., Chen, Y.-C. & Chou, P.-T. (2008). *J. Phys. Chem. C*, **112**, 9617–9622.
Shinohara, Y., Kishimoto, H., Inoue, K., Suzuki, Y., Takeuchi, A., Uesugi, K., Yagi, N., Muraoka, K., Mizoguchi, T. & Amemiya, Y. (2007). *J. Appl. Cryst.* **40**, s397–s401.
Stuhrmann, H. B. (1980). *Acta Cryst.* A**36**, 996–1001.
Su, C. H., Jeng, U., Chen, S. H., Lin, S. J., Ou, Y. T., Chuang, W.-T. & Su, A. C. (2008). *Macromolecules*, **41**, 7630–7636.
Sutton, D., Hanley, T., Knott, R. & Cookson, D. (2004). *J. Synchrotron Rad.* **11**, 505–507.
Tsuruta, H., Brennan, S., Rek, Z. U., Irving, T. C., Tompkins, W. H. & Hodgson, K. O. (1998). *J. Appl. Cryst.* **31**, 672–682.
Wang, C., Chang, L. H., Yeh, M. S., Lin, M. C., Chung, F. T., Chang, S. S., Yang, T. T. & Tsai, M. H. (2006). *Physica C*, **441**, 277–281.
Wignall, G. D. (1991). *J. Appl. Cryst.* **24**, 479–484.
Yang, H., Coombs, N., Sokolov, I. & Ozin, G. A. (1996). *Nature* (*London*), **381**, 589–592.